Received: April 2, 2019 | Accepted: May 13, 2019 | Web Released: June 4, 2019 CL-190270

Highlight Review

Progress of All-inorganic Cesium Lead-free Perovskite Solar Cells

Xiaotong Li,[1] Jinbo Wu,[1] Shenghao Wang,*[1,2] and Yabing Qi*[2]

[1]Materials Genome Institute, Shanghai University, Shanghai 200444, P. R. China
[2]Energy Materials and Surface Sciences Unit (EMSSU),
Okinawa Institute of Science and Technology Graduate University (OIST),
1919-1 Tancha, Onna-son, Okinawa 904-0495, Japan

E-mail: shenghao.wang@oist.jp (S. Wang), Yabing.Qi@OIST.jp (Y. B. Qi)

Yabing Qi is Professor and Unit Director of Energy Materials and Surface Sciences Unit (EMSSU) at Okinawa Institute of Science and Technology (OIST). Prior to his current appointment, Prof. Qi was a postdoctoral fellow at Princeton University. He received his B.S., M.Phil., and Ph.D. from Nanjing University, Hong Kong University of Science and Technology, and University of California Berkeley, respectively. His research interests include perovskite solar cells, surface sciences, energy materials, and organic electronics. (https://groups.oist.jp/emssu)

Shenghao Wang is professor in Materials Genome Institute, Shanghai University, China. He received Ph.D. from University of Tsukuba in 2013. Prior to his current appointment, he worked as a postdoctoral scholar in Prof. Yabing Qi's Unit at the OIST from 2013–2016, and then he worked in Institute of Applied Physics, University of Tsukuba from 2017–2018. His research interests include surface and interface sciences, photoemission spectroscopy techniques, and solar cells.

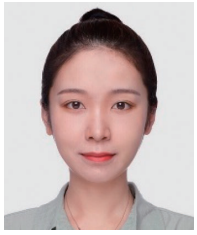

Xiaotong Li received her B.S. Degree in Polymer Materials and Engineering from Qingdao University of Science and Technology. She is currently studying for a Master's Degree in the Materials Genome Institute, Shanghai University. Her research interest focuses on lead-free perovskite solar cells.

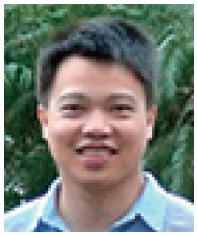

Jinbo Wu is Professor in Material Genome Institute at Shanghai University. Dr. Jinbo Wu obtained his B.S. in Applied Chemistry from Shandong University, Master and Doctoral Degree from the Hong Kong University of Science and Technology (HKUST). Prior to his current appointment, Dr. Wu was a postdoctoral fellow at HKUST and King Abdullah University of Science and Technology (KAUST). Dr. Wu's research interests include microfluidics, electrorheological fluid and evaporative guided droplet self-assembly.

Abstract

Metal halide-based perovskite solar cells (PSCs) have developed rapidly due to exceptional optoelectronic properties of perovskite materials (such as high optical absorption coefficient, long charge carrier lifetime, long diffusion length, high carrier mobility and tunable bandgaps) and low-cost fabrication processes. The record power conversion efficiency has exceeded **24**%, demonstrating the great potential for photovoltaic application. However, the lead toxicity and instability still present as major obstacles for commercialization. In principle, Pb can be replaced

with other less-toxic as well as environmentally benign metals, such as Ag, Na, Sn, Ge, Bi, Sb and Ti, to solve the toxicity issue. Replacing methylammonium (MA^+) or formamidinium (FA^+) with cesium (Cs^+) represents a promising direction to address the instability issue. Herein, we review the recent progress of all-inorganic cesium lead-free halide PSCs. At the end, we outline challenges and future directions.

Keywords: Perovskite solar cell | Lead-free | Stability

1. Introduction

Kojima *et al.* for the first time introduced $CH_3NH_3PbI_3$ perovskite into dye-sensitized solar cells, and achieved a power conversion efficiency (PCE) of 3.8% in 2009.[1] Subsequently, solid-state solar cells were fabricated by using $CH_3NH_3PbI_3$ as light absorption layer and 2,2′,7,7′-Tetrakis[*N*,*N*-di(4-methoxyphenyl)amino]-9,9′-spirobifluorene (spiro-OMeTAD) as hole transport layer (HTL) instead of iodine electrolyte resulting in a much higher PCE of 9.7%.[2] In the past several years, the device structure, interfacial engineering and processing technique of perovskite solar cells (PSCs) have been rapidly developed.[3–5] At present, the PCE has exceeded 23%.[6] Although high PCE has been achieved, PSCs still have not met the requirement for commercial applications due to the two pending major challenges: instability and toxicity.[7–9] Methylammonium lead triiodide ($MAPbI_3$) and formamidinium lead triiodide ($FAPbI_3$), which contain organic cations, have poor stability against heat, light, and moisture.[10–14] In order to improve the stability of hybrid organic-inorganic perovskites, it has been reported that all-inorganic cesium halide perovskites have become desirable candidates by replacing methylammonium (MA^+) or formamidinium (FA^+) with cesium (Cs^+) due to their excellent thermodynamic stability and resistance to humidity.[15] However, the toxicity issue is still an unresolved problem. Considering the risk, it is important to reduce or preferably eliminate lead from the photovoltaic devices. Therefore, it is of importance to develop all-inorganic lead-free PSCs.

Theoretical studies based on density functional theory (DFT) have demonstrated that the unique photovoltaic properties of lead-based perovskites can be mainly attributed to the combination of the structure symmetry and the existence of lone-pair 6 s^2 orbitals in lead, which results in direct-gap p-p transitions and appropriate bandgaps.[16,17] On the other hand, according to the geometric tolerance factor $t = (R_A + R_X)/[2^{1/2}(R_B + R_X)]$,[18,19] where R_A, R_B and R_X are the effective ion radius of A, B and X ions in the typical perovskite formula ABX_3, the size of Pb^{2+} can maintain a special symmetrical structure. For a stable structure, t ranges from 0.8 to 1.0. Substantial deviations from this range can lead to structural distortion, which weakens photovoltaic characteristics, such as poor optical absorption, wider band gap, and larger effective mass of electrons/holes.[20–22] Therefore, only limited metal ions are suitable for replacing lead ions.

In the present work, we review the development of all-inorganic cesium lead-free halide PSCs, including materials properties, fabrication methods, stability improvement, and so on. Two types of structures, namely, homovalent to lead and heterovalent to lead are mainly discussed. Also a brief overview on the current challenges and prospectives in the development of all-inorganic cesium lead-free halide PSCs is given.

2. Homovalent to Lead

2.1 $CsSnX_3$ (X = I, Br, or a Mixture of I and Br). Sn and Pb belong to the same family with lone-pair s orbitals and have similar electronic arrangement. Sn has two main oxidation states, namely, +2 state and the more stable +4 state. More impressively, Sn-based perovskites exhibit similar or sometimes even superior electronic and optical characteristics compared to Pb-based perovskites, including narrower optical bandgap and higher charge carrier mobility.[23,24] So far Sn-based perovskites with a general formula of $ASnX_3$ (A represents monovalent organic or inorganic cation) are thus the most well studied alternatives in the area of lead-free PSCs. Although most Sn-based PSCs with high PCE used organic Sn-based perovskite materials as absorbing layers, such as $MASnX_3$ and $FASnX_3$, inorganic Sn-based perovskites have great potential due to their intrinsic thermal and air stability.[25] According to t,[18,19] Cs^+ is the most promising inorganic cation to replace organic cation. $CsSnI_3$ exhibits two polymorphs: one is a yellow one-dimensional (1D) double-chain structure (*i.e.*, Y-$CsSnI_3$), the other is a black three-dimensional (3D) perovskite structure (*i.e.*, B-γ-$CsSnI_3$).[26] Y-$CsSnI_3$ has nearly no photovoltaic response under solar light illumination, while B-γ-$CsSnI_3$ (which crystallizes in the orthorhombic Pnma space group adopting a distorted 3D perovskite structure; see the panel *i* of Figure 1a) has excellent optical properties with a direct band gap of 1.3 eV and high absorption in the visible range (panel *ii* of Figure 1a).[27] Moreover, at room temperature, B-γ-$CsSnI_3$ has a fairly high hole mobility of $\sim$585 $cm^2\,V^{-1}\,s^{-1}$ [26] and low exciton binding energy of $\sim$18 meV.[28] The abovementioned excellent properties indicate that B-γ-$CsSnI_3$ has good potential as a light-absorbing material for PSCs.

2.1.1 Performance of $CsSnX_3$ PSCs: In 2012, Chen *et al.* first reported the Schottky solar cell based on $CsSnI_3$ thin film, which is synthesized by depositing $SnCl_2$ layer through e-beam evaporation and CsI layer through thermal evaporation on glass substrate followed by annealing.[29] The device consists of a simple structure of indium tin oxide (ITO)/$CsSnI_3$/Au/Ti (panel *i* of Figure 1b) showing a PCE of 0.88% (panel *ii* of Figure 1b). This low efficiency may be associated to the deteriorated film quality and the device structure.

$CsSnI_3$ easily forms intrinsic vacancies, leading to metallic conductivity.[26] These intrinsic defects lead to short carrier lifetime and severe nonradiative recombination. In order to fabricate low-defect and good-quality Sn-based perovskites films, searching for suitable additives or new film preparations may be valid solutions. In 2014, Kumar *et al.* firstly explored the addition of SnF_2 to reduce the Sn vacancies resulting in the reduced intrinsic defects and background carrier densities and hence inhibit the metallic conductivity.[30] With 20 mol % SnF_2 addition, the PCEs of 1.87% and 2.02% were achieved in the $CsSnI_3$ PSCs using spiro-OMeTAD and 4, 4′, 4″-tris(*N*,*N*-phenyl-3-methylamino)triphenylamine (m-MTDATA) as HTL, respectively. The higher efficiency is attributed to the higher recombination resistance of m-MTDATA. However, in both devices, the *V*oc (0.24 V) is low.

The substitution of I^- by Br^- in $CsSnI_3$ can change the band structure and thus effectively adjust its band gap.[25] As I^- is gradually replaced by Br^-, the bandgap of $CsSnX_3$ can be adjusted from 1.27 eV (pure $CsSnI_3$) to 1.75 eV (pure $CsSnBr_3$)

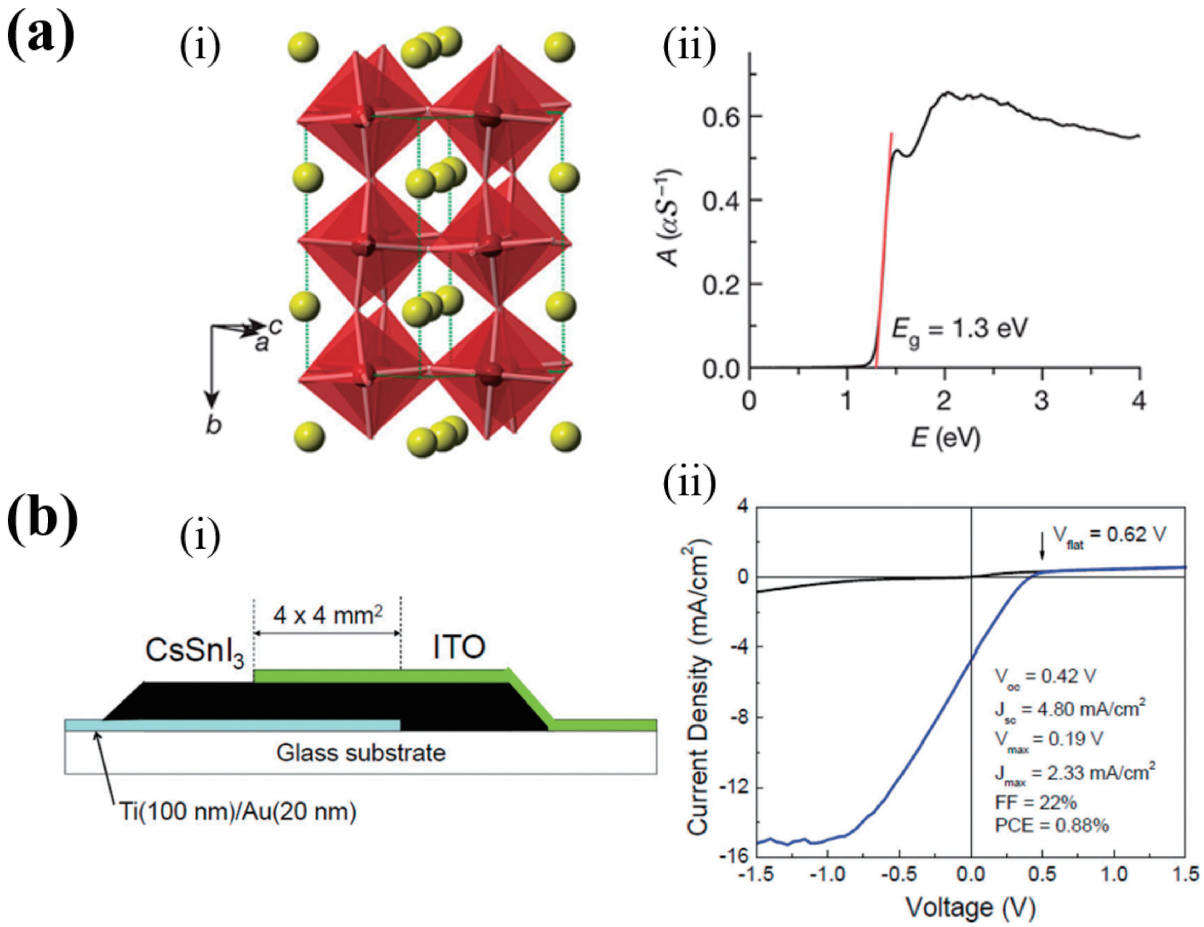

Figure 1. (a) *i*, Distorted 3D perovskite structure of $CsSnI_3$ at room temperature. Red polyhedron, $[SnI_{6/2}]^-$; yellow sphere, Cs. *ii*. $CsSnI_3$ shows a sharp absorption edge at 1.3 eV. A, absorption in units of αS^{-1}, where α is the absorption coefficient and S is the scattering coefficient. Reprinted with permission, Springer Nature, 2012.[27] (b) *i*, A schematic layer structure of the Schottky solar cell based on $CsSnI_3$. *ii*, *J-V* curves of the champion device in dark (black) and under light illumination (blue) with a power density of 50 mW/cm^2, equivalent to half of the intensity of AM 1.5 standard radiation. Reprinted with permission, AIP Publishing, 2012.[29]

with the crystal structure changing from the orthorhombic structure (pure $CsSnI_3$) to the cubic structure (pure $CsSnBr_3$) (panel *i* of Figure 2a). The increment of bandgap renders the low charge carrier density (*i.e.*, 6.32×10^{15} cm^{-3} of hole density) and increases charge recombination resistance contributing to the high V_{OC} over 0.4 V (panel *ii* of Figure 2a). However, the J_{SC} is sacrificed. It was found that $CsSnI_{2.9}Br_{0.1}$ PSC achieved the best performance (with 1.76% PCE) among $CsSnI_{3-x}Br_x$ ($0 \leq x \leq 3$) PSCs in this study.[25] It was also revealed that the PCE of 20 mol % SnF_2-$CsSnBr_3$ PSC can be improved from 0.95% to 1.28% by incorporating thicker TiO_2 (acting as electron transport layer, ETL).[25] The best $CsSnBr_3$ PSC exhibited a PCE of 2.17% with 20 mol % SnF_2 addition and 450 nm TiO_2 as ETL.[31]

A melt-synthesized $CsSnI_3$ containing high-quality large single crystal grains was reported which has superior properties compared with the polycrystalline counterpart (such as the longer carrier lifetime of 6.6 ns, the minority-carrier diffusion length close to 1 μm and the lower doping concentration of about 4.5×10^{17} cm^{-3}).[32] According to this study, the optimized $CsSnI_3$ PSC was predicted to have a PCE of 23%, exhibiting a very low surface recombination velocity (2×10^3 cm s^{-1}), similar to Pb-based PSC. To achieve high-quality perovskite films, Wang *et al.* obtained a relatively pure B-γ-$CsSnI_3$ powder by melting mixed SnI_2 and CsI in evacuated tubes and dissolving them with mixed polar solvents, followed by spin coating and annealing (panel *i* of Figure 2b).[33] The PCE of the champion B-γ-$CsSnI_3$ PSC (150 °C film annealing temperature; ~120 nm film thickness) achieved 3.31% without any additives (panel *ii* of Figure 2b). However, B-γ-$CsSnI_3$ shows very poor structural stability, and it easily converts from a cubic phase to a chain structure at room temperature leading to the poor structural stability. Because of such instability, it is difficult to obtain a pure phase and a high-quality film. A uniform, dense and pinhole-free $CsSnI_3$ film was prepared by evaporation-assisted solution method.[34] The scheme of the deposition system is shown in the panel *i* of Figure 2c. SnI_2 with SnF_2 as an additive is firstly deposited on the substrate (typically on mesoporous TiO_2) by a spin-coating method. After annealing, the SnI_2 film is transferred into the vacuum chamber for the next CsI deposition. The sample after vaporization is annealed to ensure the sufficient inter-diffusion of each component. As compared to the work in

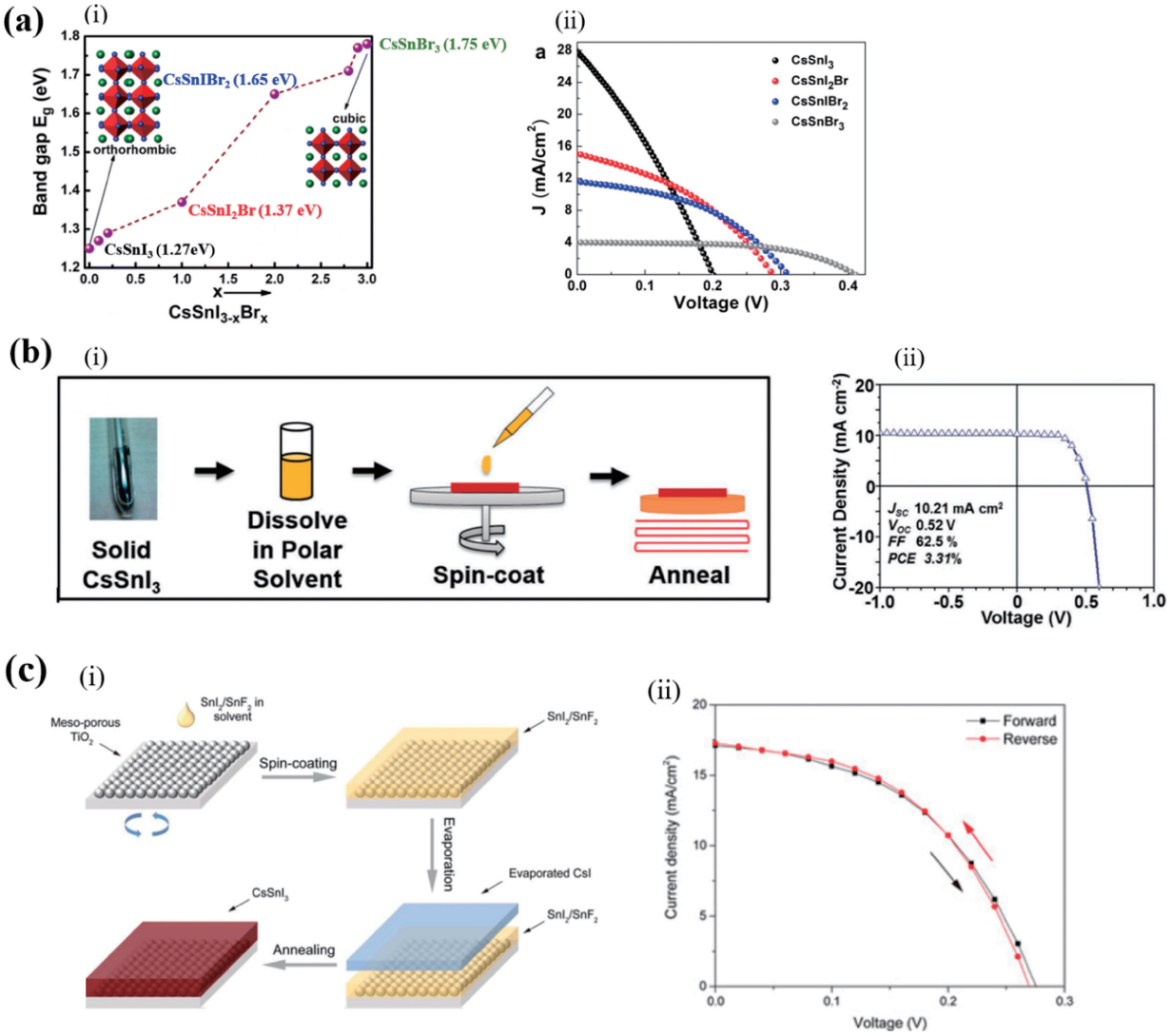

Figure 2. (a) *i*, Band gap variation as a function of the Br^- concentration. *ii*, *J*-*V* curves of $CsSnI_{1-x}Br_x$-based PSCs. Reprinted with permission, American Chemical Society, 2015.[25] (b) *i*, Schematic representation of the one-step solution fabrication of B-γ-$CsSnI_3$ thin film from solid $CsSnI_3$. *ii*, Corresponding *J*–*V* curve of the champion B-γ-$CsSnI_3$ PSC. Reprinted with permission, John Wiley and Sons, 2016.[33] (c) *i*, Schematic illustration of the evaporation-assisted solution method. *ii*, Corresponding *J*–*V* curves of the champion $CsSnI_3$ PSC in both forward and reverse directions. Reprinted with permission, John Wiley and Sons, 2018.[34]

ref 30 (*i.e.*, solution process), the rapid crystallization was retarded and the crystallization process here can be well controlled by the inter-diffusion process. Thus, the device performance improves (2.23% PCE; see the panel *ii* of Figure 2c). The device structures and the device performance of $CsSnX_3$ PSCs are summarized in Table 1.

2.1.2 Stability of $CsSnX_3$ PSCs: Although $CsSnX_3$ exceeds $MASnX_3$ or $FASnX_3$ in thermal and air stability theoretically,[27] the facile tendency of oxidization from Sn^{2+} to Sn^{4+} makes the Sn-based perovskites much more sensitive to air than the Pb analogs. For example, the absorbance of $CsSnI_3$ thin film rapidly degraded to 30% after 40 min in air (see the squared curve in the panel *i* of Figure 3a). This instability can be improved by adding SnX_2, and it was reported by Marshall *et al.* that $SnCl_2$ was the most effective additive (panel *i* of Figure 3a). The HTL-free $CsSnI_3$ PSC (with 3.56% PCE) with 10 mol % $SnCl_2$ exhibited approximately 10-fold better stability over a device with the same architecture using $MAPbI_3$ (panel *ii* of Figure 3a).[35] The improved device performance and stability stem from n-doping of the ETL by $SnCl_2$. However, Heo *et al.* reported different results, namely, they compared the additive (SnX_2) effect and found that the $SnBr_2$ is the best additive to improve the stability of $CsSnI_3$ (panel *i* of Figure 3b) and the corresponding device shows the prolonged stability of about 100 h with a high PCE of 4.3% (panel *ii* of Figure 3b) due to the passivation effect of the surface.[36] It should be commented that the device structures and the constituent layers of the devices in refs 35 and 36 are different, resulting in different effects of the additive. In addition, the fabrication condition can also affect the additive effect role. For example, Song *et al.* reported that

Table 1. The performance and stability of $CsSnX_3$ (X = I, Br, or a mixture of I and Br) PSCs.

Absorber	Device structure	V_{OC} [V]	J_{SC} [mA cm^{-2}]	PCE [%]	Device stability (Under continuous constant 1 sun simulated solar illumination)	Year	*Ref.*
20 mol % SnF_2-$CsSnI_3$	FTO/c-TiO_2/m-TiO_2/absorber/ m-MTDATA/Au	0.24	22.70	2.02	After 250 h, negligible variation of PCE (stored in glovebox)	2014	30
	FTO/c-TiO_2/m-TiO_2/absorber/spiro/Au	0.24	25.80	1.87			
10 mol % SnI_2-$CsSnI_3$	ITO/CuI/absorber/C_{60}/BCP/Al	-	-	1.5	After10 days, PCE = 1.35 % (stored in a nitrogen filled glove box: < 5 ppm O_2 and < 0.1 ppm H_2O)	2015	40
20 mol % SnF_2-$CsSnI_{2.9}Br_{0.1}$	FTO/c-TiO_2/m-TiO_2/absorber/spiro/Au	0.22	24.16	1.76	-	2015	25
20 mol % SnF_2-$CsSnI_3$	FTO/c-TiO_2/m-TiO_2/absorber/spiro/Au	0.20	27.67	1.66			
20 mol % SnF_2-$CsSnI_2Br$	FTO/c-TiO_2/m-TiO_2/absorber/spiro/Au	0.29	15.06	1.67			
20 mol % SnF_2-$CsSnIBr_2$	FTO/c-TiO_2/m-TiO_2/absorber/spiro/Au	0.31	11.57	1.56			
20 mol % SnF_2-$CsSnBr_3$	FTO/c-TiO_2/m-TiO_2/absorber/spiro/Au	0.41	3.99	0.95			
$CsSnI_3$	ITO/NiO/absorber/PCBM/Al	0.52	10.21	3.31	-	2016	33
$CsSnBr_3$	FTO/m-TiO_2/absorber/spiro/Au	0.42	9.1	2.17	-	2016	31
2.5 mol % SnF_2-$CsSnBr_3$	ITO/MoO_3/absorber/C_{60}/BCP/Ag	0.4	2.4	0.55	-	2016	41
10 mol % $SnCl_2$-$CsSnI_3$	ITO/absorber/PCBM/BCP/Al	-	-	3.56	>45min (~25 % RH, ~50 °C)	2016	35
60 mol % SnF_2+HPA- $CsSnIBr_2$	FTO/c-TiO_2/m-TiO_2/m-Al_2O_3/absorber/C	0.31	17.4	3.2	After 9 h, PCE = 3.14 % (tested by vacuum thermostatic system with a vacuum of 10^{-6} Torr at 473 K); 103 % of initial PCE after 77 days (encapsulated, ~ 25 °C, ~ 20 % RH)	2016	38
SnF_2/hydrazine-$CsSnI_3$ ($CsI : SnI_2 = 0.4$)	FTO/m-TiO_2/absorber/PTAA/ Au	0.38	25.71	4.81	-	2017	37
20 mol % SnF_2-$CsSnBr_3$	FTO/c-TiO_2/m-TiO_2/absorber/PTAA/Au	0.37	13.96	3.04	After 5 h without losing the diode characteristics (~ 40 % RH in air)	2017	42
20 mol % SnF_2/hydrazine -$CsSnI_3$	FTO/c-TiO_2/m-TiO_2/absorber/PTAA/Au	0.17	30.75	1.83	-		
$CsSnI_3$	FTO/c-TiO_2/m-TiO_2/absorber/spiro/Au	0.28	17.10	2.23	-	2018	34
10 mol % $SnBr_2$-$CsSnI_3$	FTO/c-TiO_2/absorber/PTAA/Au	0.44	18.5	4.30	After 10 h, PCE = 4.21 % (25 °C, 40 % RH)	2018	36
10 mol % $SnCl_2$-$CsSnI_3$	FTO/c-TiO_2/absorber/PTAA/Au	0.43	17.4	3.90	After 10 h, PCE = 1.80 % (25 °C, 40 % RH)		
10 mol % SnI_2-$CsSnI_3$	FTO/c-TiO_2/absorber/PTAA/Au	0.41	18	3.40	After10 h, PCE = 1.23 % (25 °C, 40 % RH)		
$CsSn_{0.5}Ge_{0.5}I_3$	FTO/PCBM/absorber/native oxide/spiro/Au	0.63	18.61	7.11	92 % of the initial PCE after 500 h (45 °C in N_2); 91 % of the initial PCE after 100 h (45 °C in air)	2019	43

FTO: fluorine doped tin oxide, RH: relative humidity, c-TiO_2: compact TiO_2, m-TiO_2: mesoporous TiO_2, TPFB: tetrakis(pentafluorophenyl)borate, HPA: hypophosphorous acid, spiro: spiro-MeOTAD, BCP: bathocuproine, PCBM: [6,6]-phenyl-C_{61}-butyric acid methyl ester, PTAA: poly[bis(4-phenyl)(2,4,6-trimethylphenyl) amine], PEDOT:PSS: poly(3,4-ethylenedioxythiophene)-poly(styrenesulfonate).

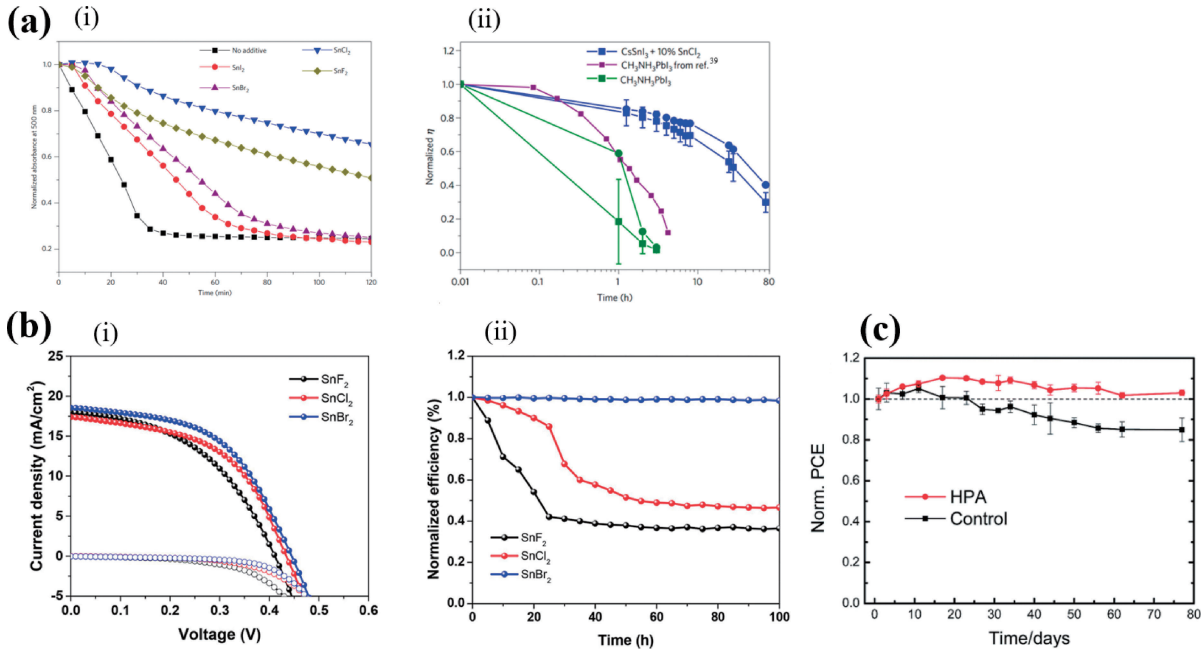

Figure 3. (a) *i*, Normalized absorbance at 500 nm for $CsSnI_3$ without and with 10 mol % of SnI_2, $SnBr_2$, $SnCl_2$ or SnF_2 additive. All films were deposited on ITO-coated glass. *ii*, Mean (squares) and champion (circles) normalized efficiency for PSCs without encapsulation tested in ambient air (at ~25% humidity and ~50 °C) under continuous 1 sun simulated solar irradiation with the structure: ITO/$CsSnI_3$ + 10 mol % $SnCl_2$/$PC_{61}BM$/BCP/Al (blue); ITO/$MAPbI_3$/$PC_{61}BM$/BCP/Al (green); ITO/$MAPbI_3$/$PC_{61}BM$/Bis-C_{60}/Ag reported in ref 39 (purple). Reprinted with permission, Springer Nature, 2016.[35] (b) *i*, *J-V* curves of the encapsulated $CsSnI_3$ PSCs with SnF_2, $SnCl_2$, and $SnBr_2$ additives. *ii*, Corresponding stability of the devices. Reprinted with permission, American Chemical Society, 2018.[36] (c) Normalized PCE of the encapsulated $CsSnIBr_2$ PSCs without and with HPA additive under ambient condition for 77 days. Reprinted with permission, Royal Society of Chemistry, 2016.[38]

adding SnF_2 in $CsSnI_3$ under a reducing vapor atmosphere of hydrazine (H_2NNH_2) can stabilize the Sn^{2+} state by playing the role of compensator and Sn^{2+} vacancy inhibitor, which effectively reduces p-type conductivity. The resulting optimized $CsSnI_3$ PSC (fabricated using molar ratios: $CsI:SnI_2 = 0.4$) achieved a maximum PCE of 4.81%.[37] Except the SnX_2, a new additive, *i.e.*, hypophosphorous acid (HPA) was used to successfully prepare the $CsSnIBr_2$ perovskite films with low Sn vacancies and stable perovskite phase.[38] The champion $CsSnIBr_2$ PSC achieved a PCE of 3.20%, more importantly, exhibiting stable PCE in 77 days (Figure 3c) and a superior thermal stability (remaining 98% of PCE) after 9 hours of continuous power output at 473 K. The stability property of $CsSnX_3$ PSCs was also summarized in Table 1.

2.2 $CsGeX_3$ (X = I, Br, Cl, or a Mixture of I and Br). Except for Sn, Pb replacement by Ge can also form a perovskite structure to satisfy the coordination on ionic size and charge balance.[15,44] Compared to $FAGeI_3$ (2.30 eV band gap) and $MAGeI_3$ (2.00 eV band gap), $CsGeI_3$ has a more suitable band gap of 1.65 eV,[45] which is larger than $CsSnI_3$ (1.3 eV[37]) due to the deeper orbital energy for Ge 4s states than that of Sn 5s states and the structural distortion of [GeI_6] octahedra.[46] It was reported that the bandgap of $CsGeI_3$ varies from 0.73 eV to 2.30 eV under different external strain,[47] which is important for understanding the effects of strain on the perovskites and guiding the experiments to improve the photovoltaic performance of the PSCs. In addition, the DFT calculation shows that $CsGeI_3$ has the best electronic and optical properties compared with $CsGeBr_3$ and $CsGeCl_3$. However, $CsGeI_3$ is inferior to $CsGe(I_{0.7}Br_{0.3})_3$ in applications due to the inferior ductility.[48] We comment that both mechanical property and the band gap should be considered for mixture $CsGe(I_{1-x}Br_x)_3$ in application.

$CsGeI_3$ is crystallized in two different space groups (with 290 °C as phase transition temperature): the lower-temperature structure R3m (panel *i* of Figure 4a) and the higher-temperature structure Pmmm (panel *ii* of Figure 4a).[49] Obviously, $CsGeI_3$ possesses the R3m structure at room temperature so high temperature treatment in the film-forming process should be avoided. In fact, in the R3m structure, Ge^{2+} and I^- form a slightly distorted cubic densest packing constituting a pyramid cluster of [GeI_3] and leading to an off-centre symmetry, which results in high optical nonlinear response.[49] In contrast to the high hole density of $CsGeI_3$ under the Ge-poor condition, $CsGeI_3$ under the Ge-rich condition is a p-type direct band gap semiconductor with reduced hole density and conductivity due to the increased concentration of the iodine vacancy.[50] However, due to the short-range potential and strong Ge-Ge covalent bond (Figure 4b), the iodine vacancy in $CsGeI_3$ is a deep electron trap, which severely restricts electron migration and thus affects V_{OC} of the PSCs.

2.2.1 Performance of $CsGeX_3$ PSCs: The research work in $CsGeI_3$ is scant. Although $CsGeI_3$ exhibits better thermal stability (with no phase transition in the range of device working temperature) compared to $MAGeI_3$ and $FAGeI_3$ (panel *i* of Figure 4c),[45] the V_{OC} of $CsGeI_3$ PSC is less than 0.1 V leading to a low PCE of only 0.11% due to the terrible film morphology

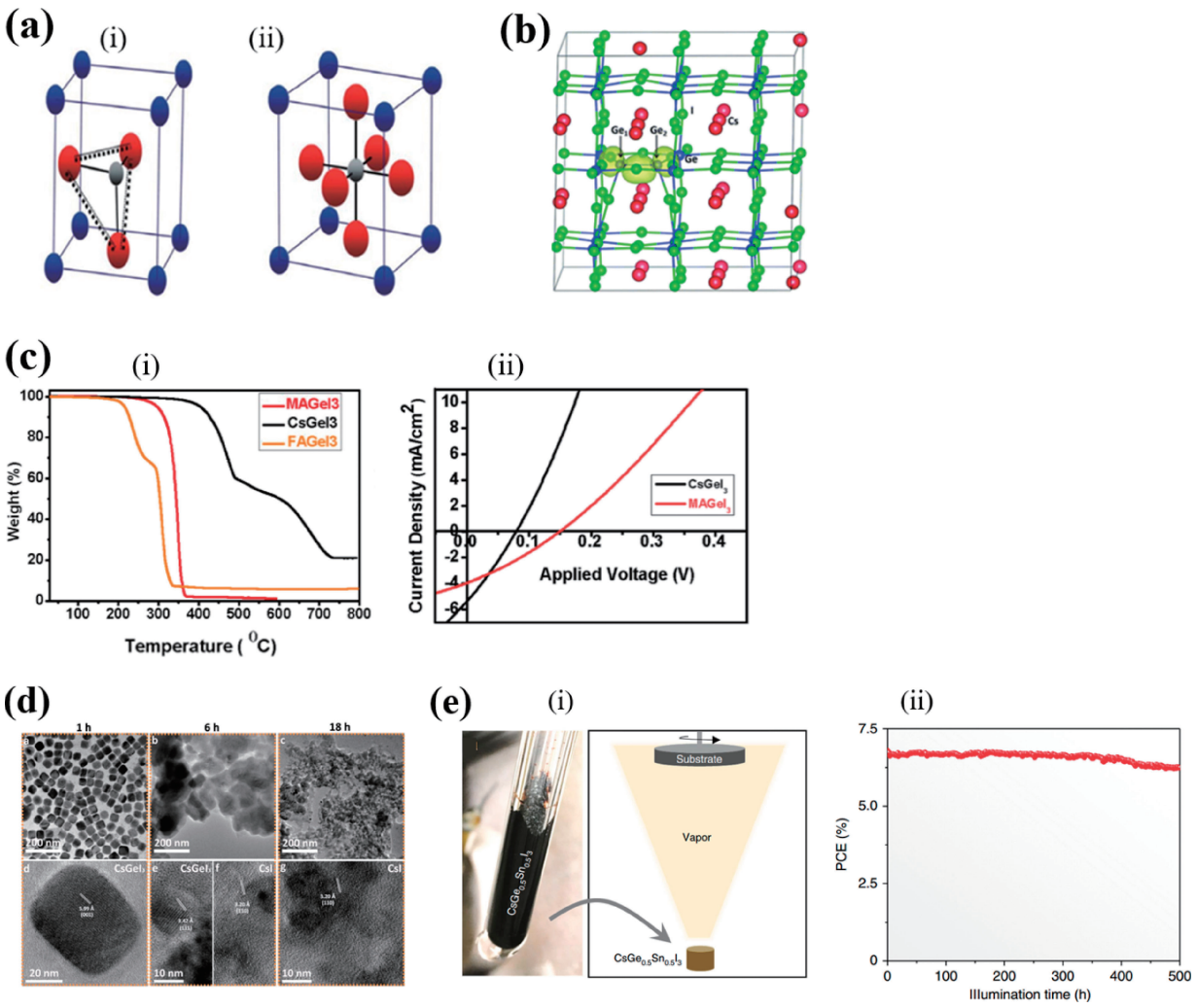

Figure 4. (a) *i*, The unit-cell structure of $CsGeI_3$ (*R*3*m*). In *R*3*m* symmetry, the Ge^{2+} ion inclines to one of the corners and a tetrahedron with a Ge^{2+} ion and three I^- ions at vertices to form a pyramidal structure. *ii*, The unit-cell structure of $CsGeI_3$ (Pmmm). In Pmmm symmetry, a Ge^{2+} ion is located at the centre of an octahedron formed by six I^- ions. Medium spheres: Cs; small spheres: Ge; large spheres: I. Reprinted with permission, IOP Publishing, 2000.[49] (b) Structure of V_I^-. The two Ge ions (Ge_1 and Ge_2) form a covalent bond. Each of them is coordinated with only two iodine ions. Reprinted with permission, Royal Society of Chemistry, 2016.[50] (c) *i*, Thermogravimetric analysis (TGA) thermogram of germanium perovskites. *ii*, *J*–*V* curves of photovoltaic devices fabricated with $CsGeI_3$ and $MAGeI_3$. Reprinted with permission, Royal Society of Chemistry, 2015.[45] (d) Transmission electron microscopy (TEM) images $CsGeI_3$ perovskite nanocubes with different exposure time at ambient condition. Reprinted with permission, John Wiley and Sons, 2018.[52] (e) *i*, Photograph of as-synthesized $CsSn_{0.5}Ge_{0.5}I_3$ perovskite solid using the melt-crystallization method and schematic illustration of the single-source evaporation method for the deposition of ultra-smooth $CsSn_{0.5}Ge_{0.5}I_3$ perovskite thin films. *ii*, PCE evolution of a typical unencapsulated PSC under continuous operation under 1-sun illumination at 45 °C in N_2 atmosphere. Reprinted with permission, Springer Nature, 2019.[43]

caused by the poor solubility in polar solvents (panel *ii* of Figure 4c). The significant efforts were made, but the V_{OC} remained low.[45,50,51] The low V_{OC} (0.46 V) has limited the maximum PCE of Ge-based solar cells to only 0.57% so far with the device structure of ITO/PEDOT:PSS/$MAGeI_{2.7}Br_{0.3}$/$PC_{70}BM$/Ag.[51]

2.2.2 Stability of $CsGeX_3$ PSCs: Recently, Wu *et al.* synthesized R3m $CsGeI_3$ perovskite colloidal nanocrystals (NCs) and studied the degradation process of the morphological change in air (shown in Figure 4d). The NCs gradually changed from single crystal $CsGeI_3$ (rhombohedral *R*3*m*) to single crystal CsI (cubic *Pm*3*m*), and then converted into polycrystalline CsI fragments.[52] This work provides insights into the instability origins by investigating morphology evolution and structure variation of $CsGeI_3$ perovskite NCs.

Surprisingly, Chen *et al.* reported a promising discovery that $CsSn_{0.5}Ge_{0.5}I_3$ formed by simply incorporating Ge^{2+} into $CsSnI_3$ exhibited high stability and a PCE up to 7.11%.[43] The panel *i* of Figure 3e shows that $CsSn_{0.5}Ge_{0.5}I_3$ powder was synthesized by the solid-state reaction between mixed solid powder precursors in evacuated Pyrex tube, and $CsSn_{0.5}Ge_{0.5}I_3$ was deposited on the substrate by a thermal evaporator. This

work indicates that PCE can be effectively enhanced by using mixed metals for replacing the pure metal of Sn in $CsSnI_3$ by solid-state reaction. The extremely high oxidation activity of Ge^{2+} [45,53] allows the rapid formation of an ultra-thin (<5 nm) uniform native-oxide passivation layer on $CsSn_{0.5}Ge_{0.5}I_3$ perovskite leading to superior stability. They further proved that the devices could run steadily for more than 500 hours under 1-sun illumination (panel *ii* of Figure 3e) with no degradation in V_{OC} and showed good reproducibility with an average PCE of 6.48%. This native-oxide passivation method provides a new solution to both improve the efficiency and stability of lead-free PSCs. In addition, it has been reported in the literature that using the GeI_2 additive in precursor can strikingly suppress the trap density of the Sn-Ge alloy perovskites, thereby rendering longer charge diffusion length (~1 μm).[54] These studies suggest alloying may help the designation of high-performance lead-free PSCs.

3. Heterovalent to Lead

3.1 Cs_2ABX_6 (A: Ag, Na; B: Bi; X = I, Br). Cesium lead-free halide double perovskites with the formula of quaternary Cs_2ABX_6 are derived from the $CsPbX_3$ perovskite structure by replacing two divalent Pb^{2+} with a pair of nontoxic heterovalent (*i.e.*, one monovalent A^+ and one trivalent B^{3+}) metal cations (Figure 5a),[55] which have recently attracted considerable interest as new alternatives to lead-halide-perovskite-based optoelectronic materials because of their non-toxicity and enhanced chemical and thermodynamic stability.[56,57] In the following, we successively summarize the progress of $Cs_2AgBiBr_6$ and Cs_2NaBiI_6 which have been used as absorbers for PSCs.

3.1.1 $Cs_2AgBiBr_6$: Many efforts have been made in the fabrication of $Cs_2AgBiBr_6$ PSCs (Table 2). The $Cs_2AgBiBr_6$ film was incorporated into PSC for the first time by Greul *et al.* via a fast spin-coating step and two important annealing steps (panel *i* of Figure 5b).[56] The first heating step is named "preheating step" where the substrate and dimethyl sulfoxide (DMSO)-based precursor solution were heated to 75 °C prior to the spin coating. Then, the hot precursor solution was spun on top of the hot substrate. The second heating step named "annealing step", was performed after the spin-coating procedure at a temperature of at least 250 °C, resulting in phase pure films. The resulting $Cs_2AgBiBr_6$ PSC exhibited a very promising PCE close to 2.5% with V_{OC} exceeding one volt (panel *ii* of Figure 5b), showing the potential of double perovskites as absorber materials. But the *J-V* curves show hysteresis, due to the trapping/de-trapping of charge carriers. By using eco-friendly anti-solvent isopropanol (IPA) technology and post-annealing process under high temperature (250 °C) (panel *i* of Figure 5c), a high quality $Cs_2AgBiBr_6$ film with ultra-smooth morphology and high crystallinity can be achieved.[58] This superior film enabled the best performing solar cell device with inverted structure ITO/Cu-NiO/$Cs_2AgBiBr_6$/C_{60}/BCP/Ag yielding a PCE of 2.23% with $V_{OC} = 1.01$ V, $J_{SC} = 3.19$ mA cm^{-2}, FF = 69.2% and no hysteresis (panel *ii* of Figure 5c). Moreover, owing to the high thermal and ambient stability of $Cs_2AgBiBr_6$, the PSC exhibited long term stability over 10 days stored in air.

In addition to the traditional solution method, Wang *et al.* successfully developed a sequential vapor deposition method to demonstrate the feasibility of high-quality double perovskite films.[55] As shown in the panel *i* of Figure 5d, AgBr is first deposited onto a dense TiO_2 coated FTO substrate. $BiBr_3$ and CsBr were then subsequently deposited on top of the AgBr film layer-by-layer. Upon subsequent thermal annealing (a two-step annealing process), a double $Cs_2AgBiBr_6$ perovskite phase was formed through diffusion reaction. The optimized PSC based on the vapor deposition of the double perovskite film showed a maximum PCE of 1.37% (panel *ii* of Figure 5d) exhibiting good device stability with reducing initial efficiency by less than 10% after 240 h storage in air. Igbari *et al*. compared vacuum-sublimation and solution-processing methods for fabricating $Cs_2AgBiBr_6$ halide double perovskite films.[57] The results showed that solution-processing could guarantee a precise composition stoichiometry to form high quality film, which leads to the optimized PCE of 2.51%. The counterpart (*i.e.*, vacuum-process) is 1.41%. Obviously, the photovoltaic performance of Cs_2AgBiX_6 solar cells is still poor, namely, a PCE of less than 3% until now.[56] Firstly, it is due to their indirect and large band gap, *i.e.*, 2.19 eV and 2.77 eV for $Cs_2AgBiBr_6$ and $Cs_2AgBiCl_6$, respectively.[59] Thus, it is necessary to find double perovskite materials which have direct band gaps. In addition, the exciton effect and electron-phonon coupling lead to undesired electron-hole recombination and hinder carrier transport.[60] Such inherent electronic properties need to be properly addressed in future double perovskite designs. For example, efficient exciton separation needs to be improved by appropriately designing the interface between the charge extraction layer and the double perovskite.

Although the performance of $Cs_2AgBiBr_6$ PSCs is worse than the PSCs homovalent to lead as discussed in ***Section*** 2, the $Cs_2AgBiBr_6$ PSCs exhibit better stability overall. The detailed stability properties of $Cs_2AgBiBr_6$ PSCs are summarized in Table 2.

3.1.2 Cs_2NaBiI_6: Another lead-free double perovskite material is Cs_2NaBiI_6 (abbreviated as CNBI), which has a band gap of 1.66 eV. CNBI can be synthesized via a facile one-step hydrothermal process.[61] CsI, NaI and BiI_3 were dissolved in hydroiodic acid at a stoichiometric molar ratio. Then the precursor was transferred to an autoclave for hydrothermal reaction to obtain CNBI. The device was fabricated by a one-step spin coating method (panel *i* of Figure 5e), and it achieved a PCE of 0.42% (panel *ii* of Figure 5e). For stability, CNBI showed negligible degradation after 5 months of storage at relative humidity of 70%.

In fact, there are other inorganic double perovskites (such as $Cs_2AgInBr_6$,[62] Cs_2AgSbX_6[63] and $Cs_2CuBiBr_6$[64]) that have potential as optical absorption materials, but they have not yet been used to prepare devices. They may bring interesting double PSCs to the photovoltaic arena. Especially, replacing Bi with In in $Cs_2AgBiBr_6$ causes direct bandgap (*i.e.*, 1.33 eV of $Cs_2AgInBr_6$).

3.2 Cs_2BX_6 (B: Sn, Ti; X: I, Br). Cs_2BX_6 derived from its $CsBX_3$ perovskite structure by removing half of the B-site cations has also received wide attention as a new type of perovskite-like structure, where B is a tetravalent metal cation (Figure 6a). Due to the absence of connectivity between the [BX_6] octahedra, the Cs_2BX_6 perovskite variants are viewed as a zero-dimensional (0D) structure, as well as double perovskite. In the following, we successively summarize the progress of

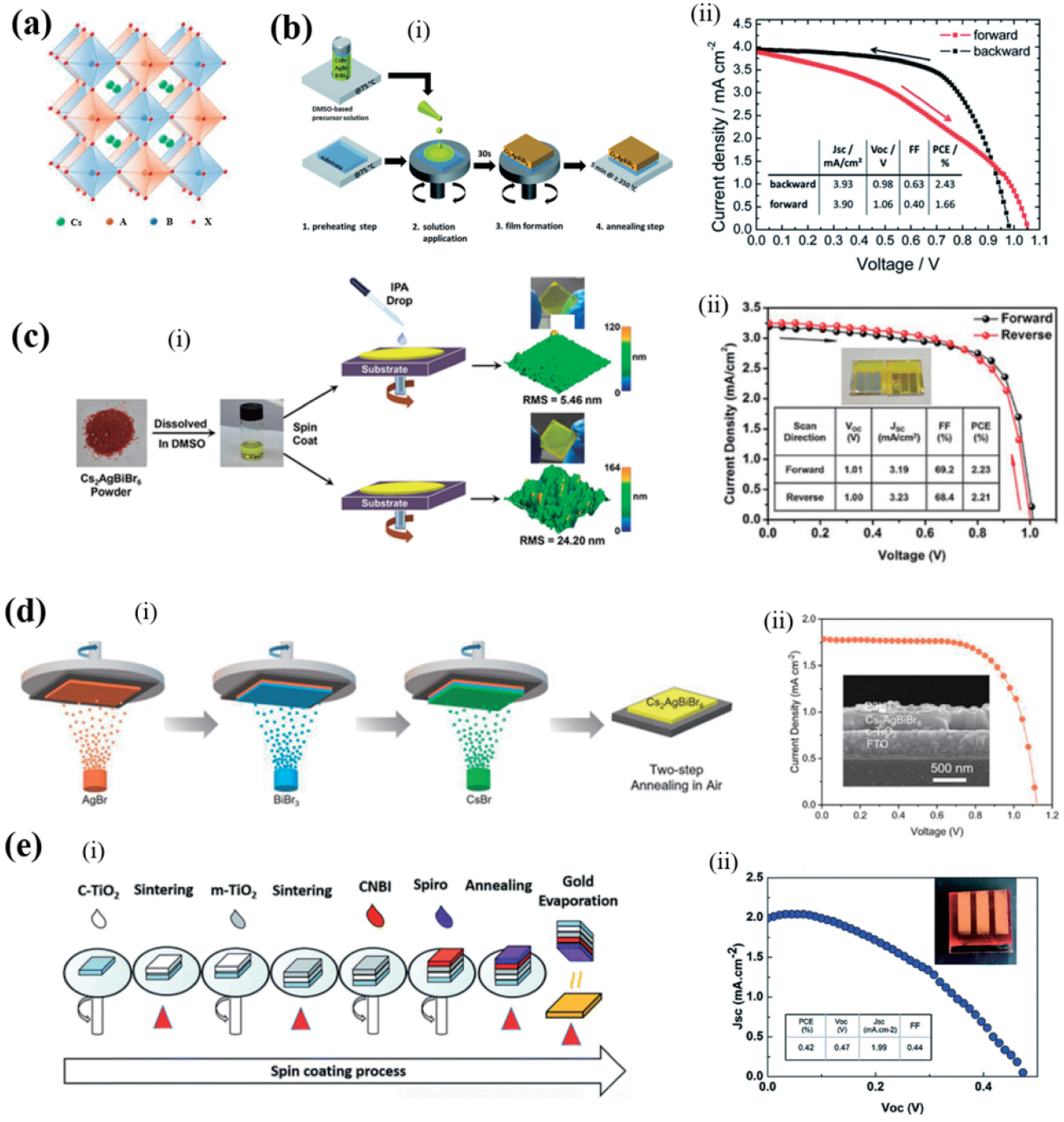

Figure 5. (a) Crystal structure of Cs_2ABX_6 double perovskite. Reprinted with permission, John Wiley and Sons, 2018.[55] (b) *i*, Schematic synthesis route for $Cs_2AgBiBr_6$ thin films. *ii*, *J-V* curve of the best performing device. Reprinted with permission, Royal Society of Chemistry, 2017.[56] (c) *i*, Schematic illustration of the spin-coating process with and without anti-solvent dropping (IPA). The morphology of the as-prepared film can be improved by IPA dropping. *ii*, *J-V* curves of forward and reverse scan directions of the best PSC. Reprinted with permission, John Wiley and Sons, 2018.[58] (d) *i*, Scheme showing the sequential vapor deposition process. *ii*, *J-V* curve of the optimized solar cell. Inset: cross-sectional scanning electron microscopy (SEM) image of the device. Reprinted with permission, John Wiley and Sons, 2018.[55] (e) *i*, Schematic illustration of Cs_2NaBiI_6 (CNBI) PSC fabrication process. *ii*, *J-V* curve of the best Cs_2NaBiI_6 PSC. Reprinted with permission, Royal Society of Chemistry, 2018.[61]

Cs_2SnI_6 and Cs_2TiBr_6 PSCs that have been investigated for photovoltaic applications.

3.2.1 Cs_2SnI_6: The Cs_2SnI_6 has a bandgap of 1.48 eV and high absorption coefficient (over $10^5\,cm^{-1}$ at 1.7 eV). It is formed by the spontaneous oxidative conversion of $CsSnI_3$ in ambient air.[68] The Cs_2SnI_6 film was for the first time adopted as a light absorber layer for a PSC obtaining an encouraging PCE of near 1% with V_{OC} of 0.51 V, J_{SC} of 5.41 mA cm^{-2} and

Table 2. The performance and stability of Cs_2ABX_6 (A: Ag, Na; B: Bi; X = I, Br) PSCs.

Absorber	Device structure	V_{OC} [V]	J_{SC} [mA cm^{-2}]	PCE [%]	Film thermal stability (No degradation at the temperature)	Device stability	Year	*Ref.*
$Cs_2AgBiBr_6$	ITO/SnO_2/absorber/P3HT/Au	1.04	1.78	1.44	-	No obvious degradation after 30 days under ambient conditions (20-30 °C, 40-60 % RH)	2018	65
	ITO/SnO_2/absorber/Au	0.95	1.50	0.86	-	Clear degradation within 1 day under ambient conditions (20-30 °C, 40-60 % RH)		
	ITO/Cu-NiO/absorber/C_{60}/BCP/Ag	1.01	3.19	2.23	100 °C for 2 h	90 % of origin PCE after 10 days	2018	58
	FTO/c-TiO_2/m-TiO_2/absorber/spiro/Au	0.98	3.93	2.43	285 °C for 5 min	No significant decay after 100 min > 25 days	2017	56
	ITO/TiO_2/absorber/spiro/Au	1.06	1.55	1.22	250 °C for 5 min	Stable PCE over 600 s	2018	66
	FTO/c-TiO_2/m-TiO_2/absorber/PTAA/Au	1.02	1.84	1.26	280 °C for 5 min	-	2018	67
	FTO/c-TiO_2/m-TiO_2/absorber/spiro/Au	0.64	2.45	0.90	280 °C for 5 min	-		
	FTO/c-TiO_2/m-TiO_2/absorber/PCPDTBT/Au	0.71	1.67	0.68	280 °C for 5 min	-		
	FTO/c-TiO_2/absorber/P3HT/Au	1.12	1.79	1.37	-	Over 90 % of initial PCE after 240 h of storage in dry box (25 °C, 7 % RH)	2018	55
	FTO/TiO_2/absorber/spiro/MoO_3/Ag	1.01	3.82	2.51	300 °C for 5 min	Over 90 % of initial PCE after 15 days	2019	57
Cs_2NaBiI_6	FTO/c-TiO_2/m-TiO_2/absorber/spiro/Au	0.47	1.99	0.42	120 °C for 2 h	Slight decrease after storage in ambient air for 14 days	2017	61

PCPDTBT: poly[2,1,3-benzothiadiazole-4,7-diyl[4,4-bis(2-ethylhexyl)-4H-cyclopenta[2,1-b:3,4-b′]dithiophene-2,6-diyl]], P3HT: poly(3-hexylthiophene-2,5-diyl).

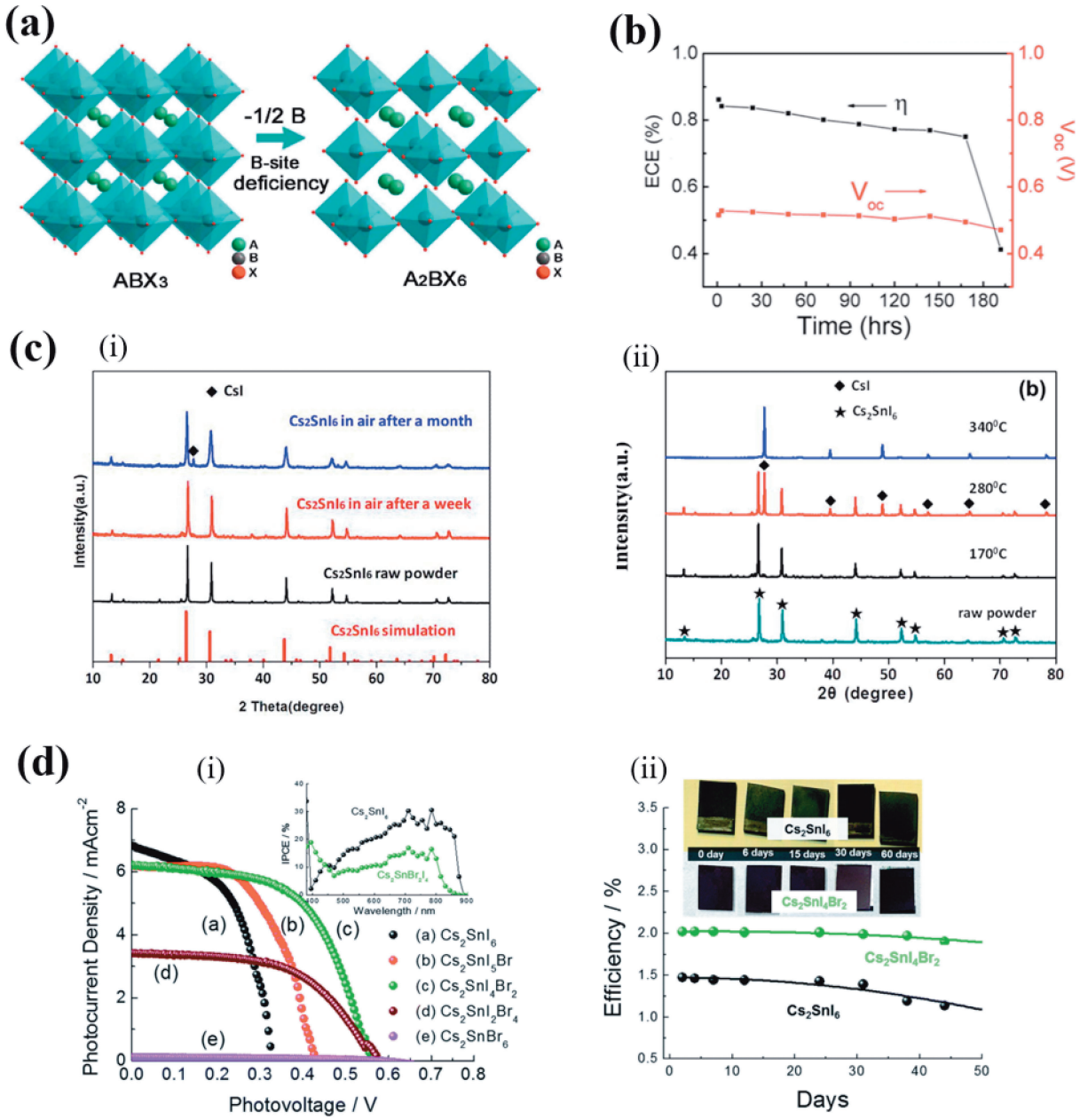

Figure 6. (a) Schematic representation of the relationship between the perovskite crystal structures of ABX_3 and B-Site deficient A_2BX_6. Reprinted with permission, American Chemical Society, 2018.[71] (b) *i*, Cs_2SnI_6-based unsealed PSC stability. Reprinted with permission, Elsevier, 2017.[68] (c) *i*, X-ray diffraction (XRD) patterns of as-prepared Cs_2SnI_6 powder in air after a month, a week, and raw powder. Vertical lines indicate the standard spectra from PDF card (51-0466). *ii*, XRD patterns after heating at different temperature (170, 280, and 340 °C). Reprinted with permission, Elsevier, 2017.[69] (d) *i*, *J-V* curves of a series of devices with different composition of $Cs_2SnI_{6-x}Br_x$ (device structure: FTO/TiO_2/Sn-TiO_2/$Cs_2SnI_{6-x}Br_x$/solid state Cs_2SnI_6 based HTL/large effective-surface-area polyaromatic hydrocarbon/FTO) structure cells. The inset shows the incident photon to charge carrier efficiency (IPCE) values for Cs_2SnI_6 (black) and $Cs_2SnBr_2I_4$ (green). *ii*, Stability properties of Cs_2SnI_6 (black), and the $Cs_2SnBr_2I_4$ (green) based solar cells for 50 days. Reprinted with permission, Royal Society of Chemistry, 2017.[70]

FF = 0.35. Though the Cs_2SnI_6 film itself is stable in dry air (RH <20%), an unsealed Cs_2SnI_6 solar cell degraded over one week (Figure 6b). Jiang *et al.* found the phase and morphology of Cs_2SnI_6 film can be maintained in high relative humidity for a week or even a month (panel *i* of Figure 6c).[69] Thermal stability measurements show that Cs_2SnI_6 is stable at about 270 °C and then decomposes into CsI and SnI_4 (panel *ii* of Figure 6c). However, they found that there are many defects in Cs_2SnI_6 film. In addition, low electron mobility and high hole effective mass were confirmed leading to the low PCE of 0.47%. This suggests that the further improvement of material quality is urgent. Lee *et al.* used two-step solution process to synthesize $Cs_2SnI_{6-x}Br_x$

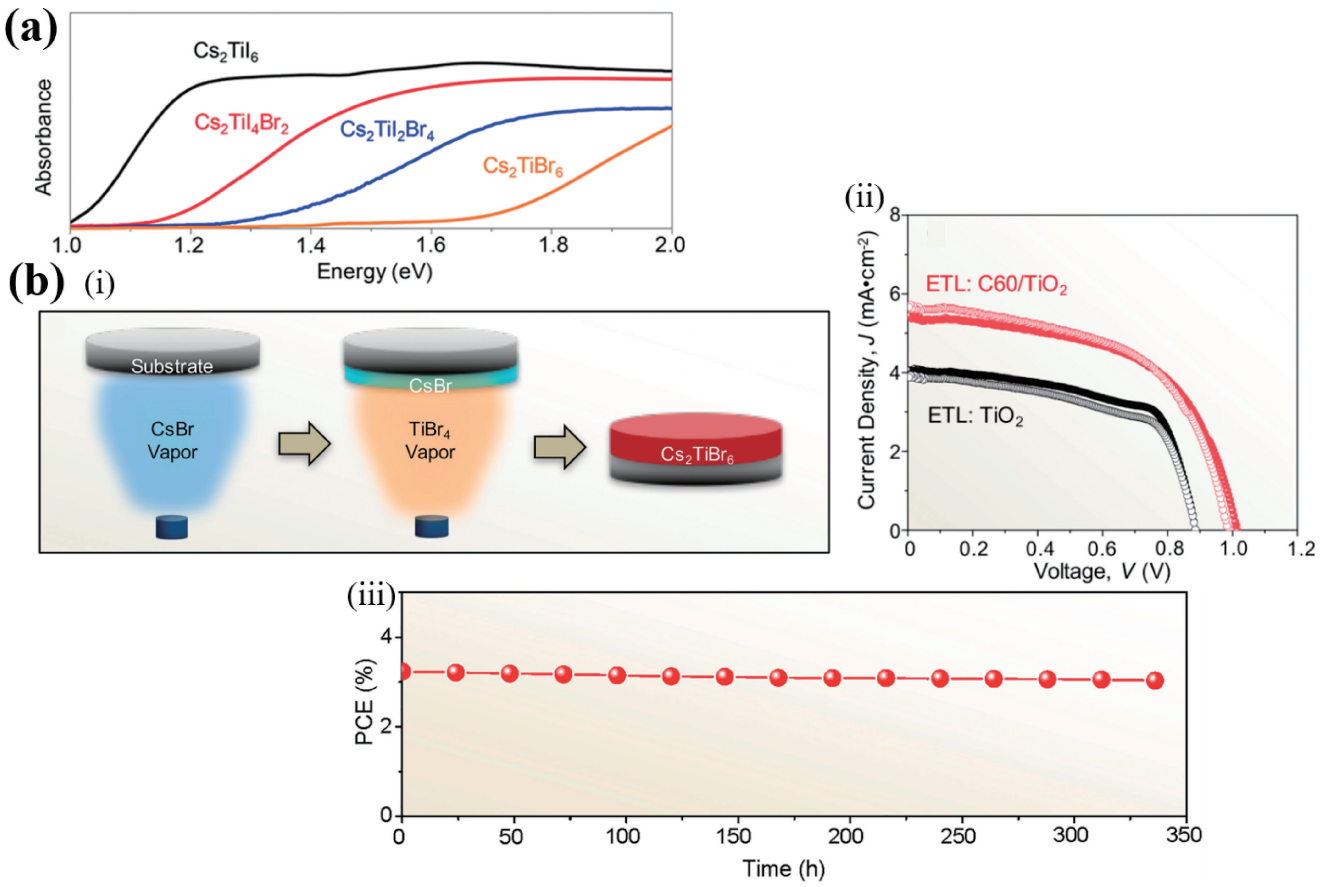

Figure 7. (a) Absorption spectra of Cs_2TiI_6, $Cs_2TiI_4Br_2$, $Cs_2TiI_2Br_4$, and Cs_2TiBr_6. Reprinted with permission, American Chemical Society, 2018.[72] (b) *i*, Schematic illustration of the vapor-based synthesis of Cs_2TiBr_6 thin film. *ii*, *J-V* curves at both forward (hollow circles) and reverse (solid circles) scans of the best PSCs without and with C_{60} interfacial layer. *iii*, Evolution of PCE of the best Cs_2TiBr_6-based PSC (unencapsulated) as a function of the storage time under environmental stress (70 °C, 30% RH, ambient light). Reprinted with permission, Elsevier, 2018.[73]

($0 < x < 3$) thin films through optimizing the annealing temperature and the annealing duration. The x value is optimized to achieve suitable properties as absorbers for light-to-charge conversion.[70] They found that the devices showed short circuits coming from the edges of the adjacent layers prepared by the standard device fabrication procedure (*i.e.*, layers were sequentially deposited forming a structure of FTO/ETL/perovskite/HTL/Au). Alternatively, they adopted a different device structure so-called "sandwich" structure as described below. Firstly, they separately fabricated the anode/perovskite part (*i.e.*, FTO/TiO_2/Sn-TiO_2/$Cs_2SnI_{6-x}Br_x$) and the cathode part (FTO/large effective-surface-area polyaromatic hydrocarbon). Then the two parts were sandwiched together using a solid state Cs_2SnI_6 based HTL. The highest PCE is 2.03% (panel *i* of Figure 6d) for a $Cs_2SnI_4Br_2$-based PSC. As shown in panel *ii* of Figure 6d, the $Cs_2SnI_4Br_2$ PSCs show stability superior to Cs_2SnI_6 PSCs. It suggests that the device stability of Cs_2SnI_6 PSCs can be improved by substitution of Br to I.

3.2.2 Cs_2TiBr_6: The bandgap of $Cs_2TiI_xBr_{6-x}$ can be tuned from 1.02 to 1.78 eV (Figure 7a).[72] Particularly, $Cs_2TiI_2Br_4$ and Cs_2TiBr_6 exhibit bandgaps of 1.38 and 1.78 eV, which are ideal for application in single-junction PSCs and tandem photovoltaics, respectively.

Recently, Chen *et al.* demonstrated that high quality Cs_2TiBr_6 film can be prepared by low temperature gas phase processes (panel *i* of Figure 7b).[73] Firstly, the CsBr layer was deposited on the substrate by thermal evaporation and the sample was placed in a chamber filled with $TiBr_4$ vapor. Correspondingly, the Cs_2TiBr_6 thin film can be obtained after 24 h. The optimal Cs_2TiBr_6 PSC with the structure of FTO/TiO_2/C_{60}/Cs_2TiBr_6/P3HT/Au showed a PCE up to 3.3% (panel *ii* of Figure 7b). The C_{60} interfacial layer not only facilitates the electron transfer from Cs_2TiBr_6 to the TiO_2 ETL, but also influences the microstructure of the as-deposited CsBr thin film and thus the formation of the Cs_2TiBr_6 thin film. In addition, the device shows good stability (panel *iii* of Figure 7b). The potential high efficiency and the superior stability as discussed above suggest that the composition and device engineering of $Cs_2TiI_xBr_{6-x}$ thin films may lead to a broader family of Ti-based perovskites for a wide range of optoelectronic application.

Except for Cs_2SnI_6 and Cs_2TiBr_6, Cs_2PdBr_6 nanocrystal (NC) has shown admirable potential in promising optoelectronic application. Cs_2PdBr_6 NC was first synthesized by a simple antisolvent method at room temperature, possessing a band gap of 1.69 eV and exhibiting sensitive photo-response behavior

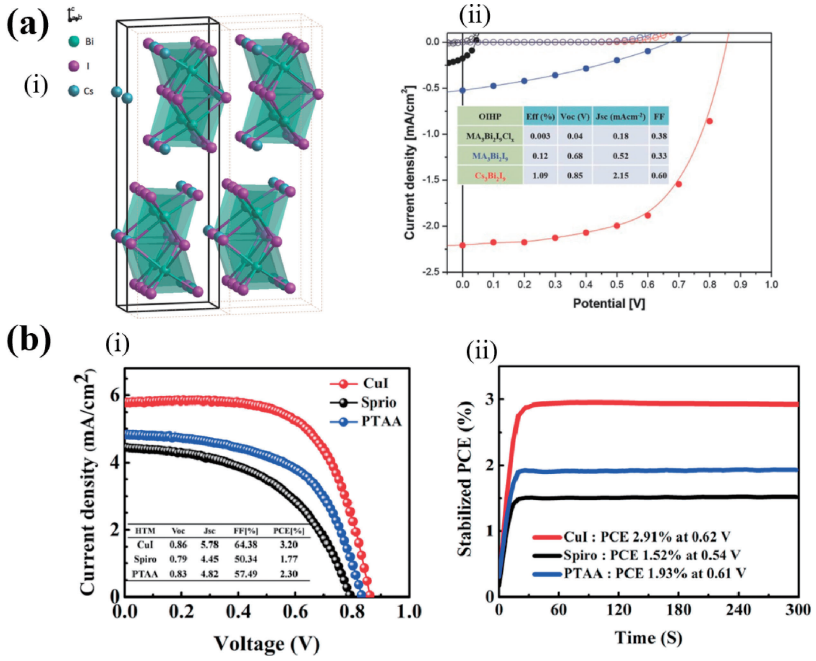

Figure 8. (a) *i*, Scheme of the $Cs_3Bi_2I_9$ structure. The unit cell is marked with the dark lines and the bismuth iodide octahedra are marked with a cyan color. *ii*, *J-V* curves of $Cs_3Bi_2I_9$, $MA_3Bi_2I_9$ and $MA_3Bi_2I_9Cl_x$ PSCs, respectively. Reprinted with permission, John Wiley and Sons, 2015.[78] (b) *i*, *J-V* curves of the $Cs_3Bi_2I_9$ PSCs with three kinds of HTL: CuI, spiro-OMeTAD and PTAA. *ii*, Steady-state PCE measured at the maximum power output point of the champion $Cs_3Bi_2I_9$ PSCs based on CuI, spiro-OMeTAD and PTAA as HTLs. Reprinted with permission, Elsevier, 2018.[80]

in photochemical tests.[71] It can also be transformed to iodide counterpart Cs_2PdI_6 NC via an anion exchange reaction. In addition, Cs_2PdBr_6 nanocrystals have high stability upon 1 sun illumination more than 1000 h, high humidity of 70% (2 months) and high temperature at 120 °C (600 h).

3.3 $Cs_3B_2I_9$ (B: Bi, Sb). $Cs_3B_2I_9$, a class of representative lead-free halide perovskites, in which B represents trivalent metal cation especially with lone-pair state (*e.g.*, Bi^{3+} and Sb^{3+}) is derived from its $CsBI_3$ parent structure by removal of 1/3 of the B-site cations, attracting significant interest as potential candidates for lead-free PSCs.[74–76] The $Cs_3B_2I_9$ perovskite have two typical polymorphs:[74] one is the so-called 0D dimer modification, which consists of an isolated face-sharing $[B_2I_9]^{3-}$ double octahedron, and the other is a two-dimensional (2D) layer modification, which can be regarded as a vacancy-ordered layered perovskite.

0D $Cs_3B_2I_9$ shows undesired optoelectronic properties for photovoltaic application because of their low structural dimensionality (corresponding to low electronic dimensionality).[77] Here, we discuss the development of vacancy-ordered 2D layered perovskites (*i.e.*, $Cs_3Bi_2I_9$ and $Cs_3Sb_2I_9$) that have been used for the light absorbing materials of PSCs.

3.3.1 $Cs_3Bi_2I_9$: The electronic structure of Bi is similar to Pb with ns^2 electrons. $Cs_3Bi_2I_9$ consists of two metal halide octahedral layers, between which the voids are filled by cations (panel *i* of Figure 8a).[78] It has rich structural changes and interesting optical and electronic properties.[78] Park *et al.* firstly used a one-step spin coating method to prepare $Cs_3Bi_2I_9$, $MA_3Bi_2I_9$, and $MA_3Bi_2I_9Cl_x$.[78] The $Cs_3Bi_2I_9$ PSC exhibited the highest performance with a PCE of more than 1% (panel *ii* of Figure 8a).

Adding excess BiI_3 in precursor solution could improve the device performance, *i.e.*, from 0.07% (no excess BiI_3) to 0.21% (with excess BiI_3), probably due to the reduction of non-radiative defects.[79] However, the 0.21% PCE is still very low compared with other cesium lead-free PSCs. The low PCE of $Cs_3Bi_2I_9$ PSCs is seriously limited by the poor photocurrent density (~0.67 mA cm^{-2}), in spite of the reasonable bandgap (~2 eV) and absorption coefficient (~1 × 10^4 cm^{-1} at 450 nm). In addition, the low PCE is also attributed to the poor charge transport resulted from the discrete nature of the double octahedra (*i.e.*, $[Bi_2I_9]^{3-}$) and subsequent bulk charge recombination. Except for the material improvement, Bai *et al.* employed different HTLs (CuI, spiro-OMeTAD and PTAA) for $Cs_3Bi_2I_9$ nanosheet based PSCs. Perhaps due to good conductivity of CuI, the $Cs_3Bi_2I_9$ PSC using CuI achieved a PCE of 3.20% (panel *i* of Figure 8b) which is the highest PCE value of double PSCs so far.[80] More importantly, the device with CuI as HTL exhibited excellent long-term stability under ambient condition (panel *ii* of Figure 8b). This work encourages us to further improve the performance of $Cs_3Bi_2I_9$ PSCs by device engineering.

3.3.2 $Cs_3Sb_2I_9$: The optoelectronic properties of both polymorphs were studied by Saparov *et al.* through DFT calculations.[81] In fact, $Cs_3Sb_2I_9$ has both the dimer and the layer modifications. While the $Cs_3Sb_2I_9$ with dimer modification has an indirect band gap of 2.40 eV, the layer modification has an almost direct band gap of 2.06 eV at the Γ point (panel *ii* of Figure 9a). The vacancy-ordered 2D layered perovskite $Cs_3Sb_2I_9$ (panel *i* of Figure 9a) exhibits improved optoelectronic properties over 0D dimer modification according to DFT calculation.[81] Compared to the dimer modification, the layer modification

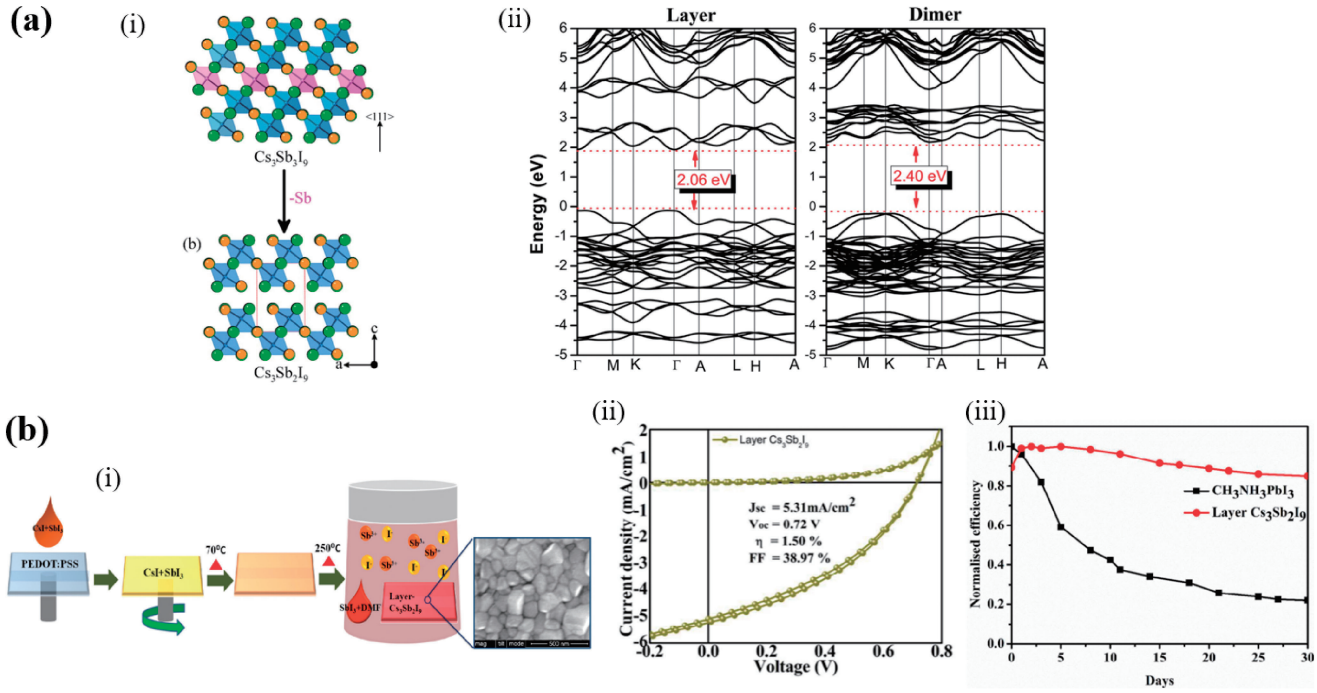

Figure 9. (a) *i*, Removal of every third Sb layer along the ⟨111⟩ direction of the perovskite structure results in the 2D layered modification of $Cs_3Sb_2I_9$. Cs and I atoms are shown as orange and green spheres, respectively; Sb coordination polyhedra are shown in blue and pink. *ii*, Calculated band structures of $Cs_3Sb_2I_9$ in layered and dimer modifications. Reprinted with permission, American Chemical Society, 2018.[81] (b) *i*, Schematic preparation process of the layered $Cs_3Sb_2I_9$, accompanied by an SEM image of the sample surface. *ii*, *J-V* curves of forward and reverse scans of layered $Cs_3Sb_2I_9$-based PSC. *iii*, Stability property of devices made with conventional Pb based perovskite (black squares) and layered $Cs_3Sb_2I_9$ (red spheres). Reprinted with permission, American Chemical Society, 2018.[82]

shows a nearly direct band gap, higher electron/hole mobility and better tolerance to defects (because of higher dielectric constants),[17,75] indicating better carrier transport as well as photovoltaic application. Although layered $Cs_3Sb_2I_9$ can exhibit potential photovoltaic behavior, solution-processing $Cs_3Sb_2I_9$ generally favors the formation of dimeric phase with poor photovoltaic properties.

Therefore, some efforts have been devoted to stabilize the layered structure of $Cs_3Sb_2I_9$ to avoid dimeric phase formation for solar cell application. Singh *et al.* prepared a layered polymorph of $Cs_3Sb_2I_9$ film with an optical band gap of 2.05 eV by vapor-assisted solution-process.[82] As shown in panel *i* of Figure 9b, a mixture of *N*,*N*-dimethylformamide (DMF) and DMSO was used as the solvent for dissolving SbI_3 and CsI. After spin-coating the precursor by the normal one step method, the sample was firstly annealed at 70 °C for 15 min to remove the solvent and then was directly moved to the bottle (covered with a cap after adding 30 wt % SbI_3 in DMF). The sample was maintained at 250 °C for 15 min in the bottle. The formed layered-$Cs_3Sb_2I_9$ PSC exhibited a PCE of 1.5% with a V_{OC} of 0.72 V (panel *ii* of Figure 9b), which is the highest reported PCE for $Cs_3Sb_2I_9$ PSCs. More importantly, the $Cs_3Sb_2I_9$ PSCs show a higher stability under ambient air as compared to $MAPbI_3$ (panel *iii* of Figure 9b).

4. Challenges and Opportunities

We summarize the best efficiencies of the cesium lead-free halide perovskite devices, as shown in Figure 10. It is obvious that they are far from the lead-based PSCs. The relatively low PCE suggests that the replacement of lead with other metal cations lowers the light-to-current conversion. Despite the inferior performance of lead-free PSCs, we still see great potential for them due to their inherent outstanding optical properties and potential good stability. Among these perovskite alternatives, replacing Pb^{2+} by Sn^{2+} and Ge^{2+} can maintain the 3D structure. However, Sn^{2+} is easy to be oxidized to Sn^{4+}. Furthermore, the $CsSnI_3$ is easy to form intrinsic vacancies, leading to metallic conductivity, and therefore short carrier lifetime and severe non-radiative recombination. Additives (such as SnX_2 and HPA) in $CsSnI_3$ can largely improve the film quality and thus the device performance. Ge-based perovskites have rarely been investigated due to the poor chemical stability of Ge^{2+} and solubility in polar solvents. Pure Ge-based PSCs have only produced a maximum PCE of 0.57% so far. Surprisingly, by simply incorporating Ge^{2+} into $CsSnI_3$ to form $CsSn_{0.5}Ge_{0.5}I_3$, the PCE and stability can be dramatically improved, revealing a feasible method to develop cesium lead-free PSCs.

The double perovskites (Cs_2ABX_6) show enormous potential as excellent candidates for lead-free perovskites because they exhibit prominent stability, especially thermal stability. However, most of the reported double perovskites, *i.e.*, $Cs_2AgBiBr_6$ show indirect and wide band gap, which are not undesirable for photovoltaic application. Thus, it is necessary to find new double perovskites possessing direct bandgap and new

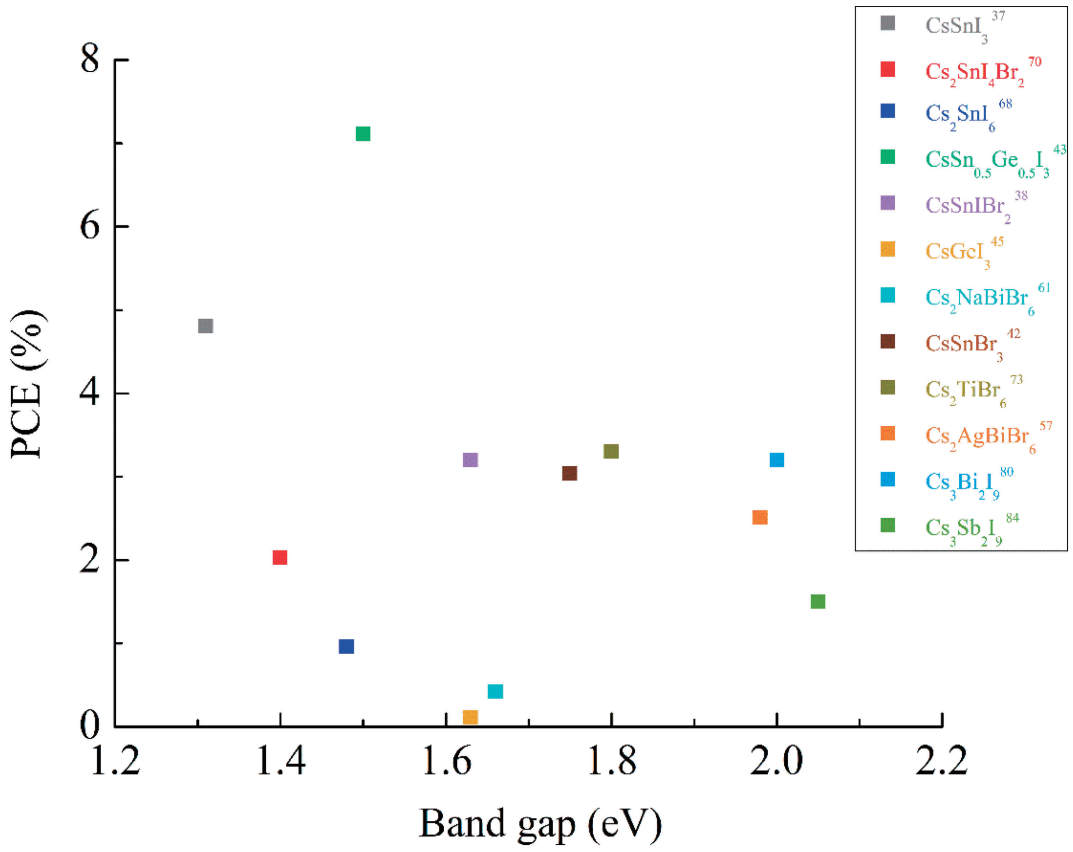

Figure 10. The best performance of cesium lead-free PSCs reported in literature. The numbers in the legend indicate reference number.

fabrication methods to prepare high-quality films. For Cs_2BX_6 double perovskites, Cs_2SnI_6 contains intrinsically deep defects that are detrimental to the PSC performance, which indicates that more efforts toward characterizing defect properties should be made. Cs_2TiBr_6 thin films-based PSCs were demonstrated showing a PCE of up to 3.3% recently, showing great potential for optoelectronic application. By further composition optimization of $Cs_2TiI_xBr_{6-x}$ and device engineering, the performance of $Cs_2TiI_xBr_{6-x}$-based PSCs may be further improved. Although Cs_2PdBr_6 shows admirable potential in promising optoelectronic application, Cs_2PdBr_6-based PSC has not been reported yet. This may be caused by the poor film formation or lack of proper fabrication method. Besides, it contains the noble element Pd, making it potentially unaffordable. The low electronic dimensionality of $Cs_3Bi_2I_9$ and $Cs_3Sb_2I_9$ leads to the poor charge transport, significantly limiting the performance of the resulting PSCs. However, they also show potential properties, especially excellent stability, which are important for photovoltaic application. In addition, the $Cs_3Bi_2I_9$ PSC achieved a PCE of 3.2% by incorporating CuI as HTL recently, which encourages us to further improveme the performance of $Cs_3Bi_2I_9$ PSCs by device engineering.

Overall, researchers have made tremendous efforts in improving both efficiency and stability of all inorganic lead-free perovskite devices. Further enhancement of efficiency of inorganic lead-free PSCs relies on material synthetic approaches, thin film preparation methods, material characterization techniques, interface engineering, and so on. Exploring new materials of lead-free perovskite with advanced opto-electronic properties and high stability will also accelerate the development of PSCs. We look forward to high efficiency and environmentally friendly lead-free PSCs making a big contribution to future renewable energy utilization.

This work was supported by the Programs for Professor of Special Appointment and Distinguished Visiting Professor (Eastern Scholar) at Shanghai Institutions of Higher Learning, and was sponsored by Shanghai Rising-Star Program (Grant No. 19QA1403800). This work was also supported by funding from the Energy Materials and Surface Sciences Unit of the Okinawa Institute of Science and Technology Graduate University, the OIST R&D Cluster Research Program, and the OIST Proof of Concept (POC) Program.

References

1 A. Kojima, K. Teshima, Y. Shirai, T. Miyasaka, *J. Am. Chem. Soc.* **2009**, *131*, 6050.
2 H.-S. Kim, C.-R. Lee, J.-H. Im, K.-B. Lee, T. Moehl, A. Marchioro, S.-J. Moon, R. Humphry-Baker, J.-H. Yum, J. E. Moser, M. Grätzel, N.-G. Park, *Sci. Rep.* **2012**, *2*, 591.
3 L. K. Ono, Y. B. Qi, *J. Phys. D: Appl. Phys.* **2018**, *51*, 093001.

4 S. Wang, T. Sakurai, W. Wen, Y. B. Qi, *Adv. Mater. Interfaces* **2018**, *5*, 1800260.
5 L. K. Ono, Y. B. Qi, *J. Phys. Chem. Lett.* **2016**, *7*, 4764.
6 https://www.nrel.gov/pv/assets/pdfs/best-research-cell-efficiencies-190416.pdf.
7 L. Qiu, L. K. Ono, Y. B. Qi, *Mater. Today Energy* **2018**, *7*, 169.
8 L. K. Ono, N.-G. Park, K. Zhu, W. Huang, Y. B. Qi, *ACS Energy Lett.* **2017**, *2*, 1749.
9 L. K. Ono, Y. B. Qi, S. Liu, *Joule* **2018**, *2*, 1961.
10 M. Kulbak, S. Gupta, N. Kedem, I. Levine, T. Bendikov, G. Hodes, D. Cahen, *J. Phys. Chem. Lett.* **2016**, *7*, 167.
11 J. K. Nam, S. U. Chai, W. Cha, Y. J. Choi, W. Kim, M. S. Jung, J. Kwon, D. Kim, J. H. Park, *Nano Lett.* **2017**, *17*, 2028.
12 S. Wang, Y. Jiang, E. J. Juarez-Perez, L. K. Ono, Y. B. Qi, *Nat. Energy* **2016**, *2*, 16195.
13 E. J. Juarez-Perez, Z. Hawash, S. R. Raga, L. K. Ono, Y. B. Qi, *Energy Environ. Sci.* **2016**, *9*, 3406.
14 E. J. Juarez-Perez, L. K. Ono, M. Maeda, Y. Jiang, Z. Hawash, Y. B. Qi, *J. Mater. Chem. A* **2018**, *6*, 9604.
15 C. C. Stoumpos, C. D. Malliakas, M. G. Kanatzidis, *Inorg. Chem.* **2013**, *52*, 9019.
16 B. Yim, Y. Nagata, Y. Maeda, *J. Phys. Chem. A* **2002**, *106*, 104.
17 R. E. Brandt, V. Stevanović, D. S. Ginley, T. Buonassisi, *MRS Commun.* **2015**, *5*, 265.
18 V. M. Goldschmidt, *Ber. Dtsch. Chem. Ges.* **1927**, *60*, 1263.
19 A. Amat, E. Mosconi, E. Ronca, C. Quarti, P. Umari, M. K. Nazeeruddin, M. Grätzel, F. De Angelis, *Nano Lett.* **2014**, *14*, 3608.
20 W.-J. Yin, T. Shi, Y. Yan, *Adv. Mater.* **2014**, *26*, 4653.
21 C. C. Stoumpos, L. Frazer, D. J. Clark, Y. S. Kim, S. H. Rhim, A. J. Freeman, J. B. Ketterson, J. I. Jang, M. G. Kanatzidis, *J. Am. Chem. Soc.* **2015**, *137*, 6804.
22 B. Saparov, J.-P. Sun, W. Meng, Z. Xiao, H.-S. Duan, O. Gunawan, D. Shin, I. G. Hill, Y. Yan, D. B. Mitzi, *Chem. Mater.* **2016**, *28*, 2315.
23 F. Giustino, H. J. Snaith, *ACS Energy Lett.* **2016**, *1*, 1233.
24 A. Abate, *Joule* **2017**, *1*, 887.
25 D. Sabba, H. K. Mulmudi, R. R. Prabhakar, T. Krishnamoorthy, T. Baikie, P. P. Boix, S. Mhaisalkar, N. Mathews, *J. Phys. Chem. C* **2015**, *119*, 1763.
26 I. Chung, J. H. Song, J. Im, J. Androulakis, C. D. Malliakas, H. Li, A. J. Freeman, J. T. Kenney, M. G. Kanatzidis, *J. Am. Chem. Soc.* **2012**, *134*, 8579.
27 I. Chung, B. Lee, J. He, R. P. H. Chang, M. G. Kanatzidis, *Nature* **2012**, *485*, 486.
28 Z. Chen, C. Yu, K. Shum, J. J. Wang, W. Pfenninger, N. Vockic, J. Midgley, J. T. Kenney, *J. Lumin.* **2012**, *132*, 345.
29 Z. Chen, J. J. Wang, Y. Ren, C. Yu, K. Shum, *Appl. Phys. Lett.* **2012**, *101*, 093901.
30 M. H. Kumar, S. Dharani, W. L. Leong, P. P. Boix, R. R. Prabhakar, T. Baikie, C. Shi, H. Ding, R. Ramesh, M. Asta, M. Graetzel, S. G. Mhaisalkar, N. Mathews, *Adv. Mater.* **2014**, *26*, 7122.
31 S. Gupta, T. Bendikov, G. Hodes, D. Cahen, *ACS Energy Lett.* **2016**, *1*, 1028.
32 B. Wu, Y. Zhou, G. Xing, Q. Xu, H. F. Garces, A. Solanki, T. W. Goh, N. P. Padture, T. C. Sum, *Adv. Funct. Mater.* **2017**, *27*, 1604818.
33 N. Wang, Y. Zhou, M.-G. Ju, H. F. Garces, T. Ding, S. Pang, X. C. Zeng, N. P. Padture, X. W. Sun, *Adv. Energy Mater.* **2016**, *6*, 1601130.
34 P. Zhu, C. Chen, S. Gu, R. Lin, J. Zhu, *Sol. RRL* **2018**, *2*, 1700224.
35 K. P. Marshall, M. Walker, R. I. Walton, R. A. Hatton, *Nat. Energy* **2016**, *1*, 16178.
36 J. H. Heo, J. Kim, H. Kim, S. H. Moon, S. H. Im, K.-H. Hong, *J. Phys. Chem. Lett.* **2018**, *9*, 6024.
37 T.-B. Song, T. Yokoyama, S. Aramaki, M. G. Kanatzidis, *ACS Energy Lett.* **2017**, *2*, 897.
38 W. Li, J. Li, J. Li, J. Fan, Y. Mai, L. Wang, *J. Mater. Chem. A* **2016**, *4*, 17104.
39 Y. Zhang, X. Hu, L. Chen, Z. Huang, Q. Fu, Y. Liu, L. Zhang, Y. Chen, *Org. Electron.* **2016**, *30*, 281.
40 K. P. Marshall, R. I. Walton, R. A. Hatton, *J. Mater. Chem. A* **2015**, *3*, 11631.
41 D. Moghe, L. Wang, C. J. Traverse, A. Redoute, M. Sponseller, P. R. Brown, V. Bulović, R. R. Lunt, *Nano Energy* **2016**, *28*, 469.
42 T.-B. Song, T. Yokoyama, C. C. Stoumpos, J. Logsdon, D. H. Cao, M. R. Wasielewski, S. Aramaki, M. G. Kanatzidis, *J. Am. Chem. Soc.* **2017**, *139*, 836.
43 M. Chen, M.-G. Ju, H. F. Garces, A. D. Carl, L. K. Ono, Z. Hawash, Y. Zhang, T. Shen, Y. Qi, R. L. Grimm, D. Pacifici, X. C. Zeng, Y. Zhou, N. P. Padture, *Nat. Commun.* **2019**, *10*, 16.
44 W. Li, Z. Wang, F. Deschler, S. Gao, R. H. Friend, A. K. Cheetham, *Nat. Rev. Mater.* **2017**, *2*, 16099.
45 T. Krishnamoorthy, H. Ding, C. Yan, W. L. Leong, T. Baikie, Z. Zhang, M. Sherburne, S. Li, M. Asta, N. Mathews, S. G. Mhaisalkar, *J. Mater. Chem. A* **2015**, *3*, 23829.
46 Z. Xiao, Z. Song, Y. Yan, *Adv. Mater.* **2019**, 1803792.
47 D. Liu, Q. Li, H. Jing, K. Wu, *RSC Adv.* **2019**, *9*, 3279.
48 M. Roknuzzaman, K. Ostrikov, H. Wang, A. Du, T. Tesfamichael, *Sci. Rep.* **2017**, *7*, 14025.
49 L.-C. Tang, C.-S. Chang, L.-C. Tang, J. Y. Huang, *J. Phys.: Condens. Matter* **2000**, *12*, 9129.
50 W. Ming, H. Shi, M.-H. Du, *J. Mater. Chem. A* **2016**, *4*, 13852.
51 I. Kopacic, B. Friesenbichler, S. F. Hoefler, B. Kunert, H. Plank, T. Rath, G. Trimmel, *ACS Appl. Energy Mater.* **2018**, *1*, 343.
52 X. Wu, W. Song, Q. Li, X. Zhao, D. He, Z. Quan, *Chem.—Asian J.* **2018**, *13*, 1654.
53 S. F. Hoefler, G. Trimmel, T. Rath, *Monatsh. Chem.* **2017**, *148*, 795.
54 C. H. Ng, K. Nishimura, N. Ito, K. Hamada, D. Hirotani, Z. Wang, F. Yang, S. Iikubo, Q. Shen, K. Yoshino, T. Minemoto, S. Hayase, *Nano Energy* **2019**, *58*, 130.
55 M. Wang, P. Zeng, S. Bai, J. Gu, F. Li, Z. Yang, M. Liu, *Sol. RRL* **2018**, *2*, 1800217.
56 E. Greul, M. L. Petrus, A. Binek, P. Docampo, T. Bein, *J. Mater. Chem. A* **2017**, *5*, 19972.
57 F. Igbari, R. Wang, Z.-K. Wang, X.-J. Ma, Q. Wang, K.-L. Wang, Y. Zhang, L.-S. Liao, Y. Yang, *Nano Lett.* **2019**, *19*, 2066.
58 W. Gao, C. Ran, J. Xi, B. Jiao, W. Zhang, M. Wu, X. Hou, Z. Wu, *ChemPhysChem* **2018**, *19*, 1696.

59 E. T. McClure, M. R. Ball, W. Windl, P. M. Woodward, *Chem. Mater.* **2016**, *28*, 1348.
60 R. Kentsch, M. Scholz, J. Horn, D. Schlettwein, K. Oum, T. Lenzer, *J. Phys. Chem. C* **2018**, *122*, 25940.
61 C. Zhang, L. Gao, S. Teo, Z. Guo, Z. Xu, S. Zhao, T. Ma, *Sustainable Energy Fuels* **2018**, *2*, 2419.
62 J. Xu, J.-B. Liu, B.-X. Liu, B. Huang, *J. Phys. Chem. Lett.* **2017**, *8*, 4391.
63 Z. Xiao, K.-Z. Du, W. Meng, J. Wang, D. B. Mitzi, Y. Yan, *J. Am. Chem. Soc.* **2017**, *139*, 9409.
64 H.-J. Feng, W. Deng, K. Yang, J. Huang, X. C. Zeng, *J. Phys. Chem. C* **2017**, *121*, 4471.
65 C. Wu, Q. Zhang, Y. Liu, W. Luo, X. Guo, Z. Huang, H. Ting, W. Sun, X. Zhong, S. Wei, S. Wang, Z. Chen, L. Xiao, *Adv. Sci.* **2018**, *5*, 1700759.
66 W. Ning, F. Wang, B. Wu, J. Lu, Z. Yan, X. Liu, Y. Tao, J.-M. Liu, W. Huang, M. Fahlman, L. Hultman, T. C. Sum, F. Gao, *Adv. Mater.* **2018**, *30*, 1706246.
67 M. Pantaler, K. T. Cho, V. I. E. Queloz, I. García Benito, C. Fettkenhauer, I. Anusca, M. K. Nazeeruddin, D. C. Lupascu, G. Grancini, *ACS Energy Lett.* **2018**, *3*, 1781.
68 X. Qiu, B. Cao, S. Yuan, X. Chen, Z. Qiu, Y. Jiang, Q. Ye, H. Wang, H. Zeng, J. Liu, M. G. Kanatzidis, *Sol. Energy Mater. Sol. Cells* **2017**, *159*, 227.
69 Y. Jiang, H. Zhang, X. Qiu, B. Cao, *Mater. Lett.* **2017**, *199*, 50.
70 B. Lee, A. Krenselewski, S. I. Baik, D. N. Seidman, R. P. H. Chang, *Sustainable Energy Fuels* **2017**, *1*, 710.
71 L. Zhou, J.-F. Liao, Z.-G. Huang, X.-D. Wang, Y.-F. Xu, H.-Y. Chen, D.-B. Kuang, C.-Y. Su, *ACS Energy Lett.* **2018**, *3*, 2613.
72 M.-G. Ju, M. Chen, Y. Zhou, H. F. Garces, J. Dai, L. Ma, N. P. Padture, X. C. Zeng, *ACS Energy Lett.* **2018**, *3*, 297.
73 M. Chen, M.-G. Ju, A. D. Carl, Y. Zong, R. L. Grimm, J. Gu, X. C. Zeng, Y. Zhou, N. P. Padture, *Joule* **2018**, *2*, 558.
74 J.-H. Chang, T. Doert, M. Ruck, *Acta Crystallogr. C Struct. Chem.* **2016**, *72*, 966.
75 P. C. Harikesh, H. K. Mulmudi, B. Ghosh, T. W. Goh, Y. T. Teng, K. Thirumal, M. Lockrey, K. Weber, T. M. Koh, S. Li, S. Mhaisalkar, N. Mathews, *Chem. Mater.* **2016**, *28*, 7496.
76 B. Jiang, K. Kani, M. Iqbal, H. Abe, T. Kimura, M. S. A. Hossain, O. Anjaneyulu, J. Henzie, Y. Yamauchi, *Chem. Mater.* **2018**, *30*, 428.
77 F. Igbari, Z.-K. Wang, L.-S. Liao, *Adv. Energy Mater.* **2019**, *9*, 1803150.
78 B.-W. Park, B. Philippe, X. Zhang, H. Rensmo, G. Boschloo, E. M. J. Johansson, *Adv. Mater.* **2015**, *27*, 6806.
79 B. Ghosh, B. Wu, H. K. Mulmudi, C. Guet, K. Weber, T. C. Sum, S. Mhaisalkar, N. Mathews, *ACS Appl. Mater. Interfaces* **2018**, *10*, 35000.
80 F. Bai, Y. Hu, Y. Hu, T. Qiu, X. Miao, S. Zhang, *Sol. Energy Mater. Sol. Cells* **2018**, *184*, 15.
81 B. Saparov, F. Hong, J.-P. Sun, H.-S. Duan, W. Meng, S. Cameron, I. G. Hill, Y. Yan, D. B. Mitzi, *Chem. Mater.* **2015**, *27*, 5622.
82 A. Singh, K. M. Boopathi, A. Mohapatra, Y. F. Chen, G. Li, C. W. Chu, *ACS Appl. Mater. Interfaces* **2018**, *10*, 2566.

